Int. J. Electrochem. Sci., 17 **(2022)** Article Number: 221169, doi: 10.20964/2022.11.87

International Journal of
ELECTROCHEMICAL
SCIENCE
www.electrochemsci.org

Synthesis and Electrochemical Characterizations of Concentration-Gradient Structure Nickel-Rich Cathode Materials

Yi-Lin Wu[1], *Chun-Chieh Lan*[1], *Mao-Huang Liu*[1,*], *Jin-Ming Chen*[2], *Shih-Chieh Liao*[2] , *Chia-Erh Liu*[2]

[1] Department of Chemistry, Fu Jen Catholic University, New Taipei City, Taiwan 24205
[2] Material and Chemical Research Laboratories, Industrial Technology Research Institute, HsinChu, Taiwan 31040
[*]E-Mail: 061355@mail.fju.edu.tw

Received: 12 August 2022 / *Accepted:* 1 October 2022 / *Published:* 20 October 2022

A nickel-rich cathode material with a continuous concentration-gradient structure of $LiNi_{0.9}Co_{0.05}Mn_{0.05}O_2$ (CG-LNCMO) was successfully synthesized via a two-step co-precipitation process. According to careful examinations conducted via scanning electron microscopy/energy-dispersive spectroscopy (SEM/EDS) and inductively coupled plasma-optical emission spectroscopy (ICP-OES), CG-LNCMO material has the primary particles with different chemical compositions from the surface to the core of the secondary particles. Moreover, CG-LNCMO has better electrochemical characteristics, as a result of a higher manganese content on the surface of the material, which serves to stabilize the material structure and reduce the side reactions between the material and electrolyte. Compared with the average composition of $LiNi_{0.9}Co_{0.05}Mn_{0.05}O_2$ (AC-LNCMO), the concentration-gradient cathode material has the structural stability, high capacity, and good electrochemical performances to make it a plausible candidate for application in high-performance lithium-ion batteries.

Keywords: lithium-ion batteries, nickel-rich cathode, concentration-gradient, co-precipitation

1. INTRODUCTION

Environmental protection and SDGs (Sustainable Development Goals) are progressively becoming valued, and most countries in the world are adopting policies of reducing carbon emissions and promoting forms of renewable energy. The efficiency of energy storage systems plays a crucial role in the process of replacing fueled cars with electric vehicles. Lithium-ion secondary batteries possess the properties of high-energy density, high working voltage, and low self-discharge, which have made them the superior choice among various batteries [1]. The outstanding discharge performance and durable cycle life of $LiCoO_2$ made it one of the earliest cathode materials. However, due to its limited capacity (~140 mAhg^{-1}), when $LiCoO_2$ is operated at higher potential, the excess charge/discharge process can cause an irreversible phase change in the crystal structure, which shortens its cycle life. Thus, researchers are striving to find other cathode materials that could fulfill the requirements of high capacity [2-4].

$LiNiO_2$ has drawn much attention as a potential replacement for $LiCoO_2$ due to its high energy density and low cost. Unfortunately, the synthesis of $LiNiO_2$ is difficult, and its structural and thermal stability is poor [5-7]. Some researchers have begun doping Co and Mn into $LiNiO_2$ to partially replace Ni to improve structural stability. The properties of a three-element cathode material such as $LiNi_xCo_yMn_{1-x-y}O_2$ are greatly diversified, because the ratios of Ni, Co and Mn vary. Most researchers have chosen nickel-rich cathode material to increase the overall energy density for electric vehicles [8-15].

Raising the proportion of nickel in cathode material, however, tends to jeopardize the material stability and battery safety. It is because the cation-mixing, structurally unstable and Ni^{4+} reacting with electrolytes are all likely to occur with nickel-rich cathode material [15]. A couple of modifications that can be used to protect the integrity of cathode material such as doping certain metal inside to stabilize the structure, or coating a nanoscale metal oxide layer on the surface to prevent a reaction with electrolytes. Both modification methods, however, tend to reduce the capacity, which contradicts the purpose of developing cathode material with high-energy density [16-22].

The Li-ion batteries of today demand material with higher capacity and superior electrochemical performance. With the present study, the goal was to redesign the structure of the nickel-rich cathode material $LiNiCoMnO_2$. High capacity and structural stability were achieved via the use of an element-concentration gradient. A non-homogeneous particle structure was realized via control of the chemical composition and synthetic processes. The element composition on the surface of a material particle tends to possess a stable structure, whereas the element composition in the core of a particle tends to be higher in capacity. Since there is a continuous concentration gradient, there is no core-shell interface inside the particles of a material, which eliminates the junction resistance between two different compositions [23-29].

In addition to the use of nickel-rich material, both high packing density and better electrode kinetics would also improve the energy density of batteries. To meet these criteria, it is necessary to synthesize spherical material particles with a nano-structure. Nano-structured spherical cathode material was obtained via co-precipitation with controlled nucleation and nucleus growth through the adjustment of reaction conditions such as temperature, concentration, reaction time, and precipitation reagent [10-12,14,24,25,30,31].

This work presents the synthesis of nickel-rich cathode material, $LiNi_{0.9}Co_{0.05}Mn_{0.05}O_2$, with a continuous concentration gradient [32-33]. Not only improve the structural stability on the particle surface but also maintain the capacity of cathode material. The material developed in this study is one step closer to the ideal high energy density cathode material by balancing both stability and capacity.

2. EXPERIMENTAL

2.1. Synthesis of Cathode Materials

The precursor of the cathode material consisted of 95% mol. $Ni_{0.95}Co_{0.05}(OH)_2$ coated with 5% mol. $Mn(OH)_2$ that was synthesized via co-precipitation. The 1.6 M ion solution contained $NiSO_4·6H_2O$ and $CoSO_4·7H_2O$ in a molar ratio of 95:5. An aqueous solution of 3.84 M NaOH was used as a precipitant. The chelating reagent consisted of 7.8 M NH_4OH in water. First, 1,000 mL of a 1.2 M NH_4OH aqueous solution was placed into a two-liter reaction tank with a stirrer set to 2,000 rpm. The temperature of the reaction solution was kept at 60 ℃. Ion solution and chelating reagent were added to the reaction tank in a controlled ratio using a peristaltic pump. The pH of the reaction solution was maintained at 10.5 by controlling the addition of precipitant using feedback from a pH meter. The reaction time was set at 24 hours. The powder of the precursor was collected through suction filtration. The powder of the $Ni_{0.95}Co_{0.05}(OH)_2$ precursor was obtained after drying at 80 ℃. The precursor powder was then suspended in an aqueous solution of NH_4OH that was stirred at a speed of 2,000 rpm and maintained at 60 ℃. Aqueous solutions of 0.283 M $MnSO_4$, 1.95 M NH_4OH, and 0.68 M NaOH were gradually added to the reactor via a peristaltic pump. The solution in the reactor was maintained at pH 9.5 and purged with nitrogen. After 1 hour of reaction, the suspended solution was filtered, washed, and dried. The resultant powders were 5% mol. of $Mn(OH)_2$ coated with 95% mol. of the $Ni_{0.95}Co_{0.05}(OH)_2$ precursor.

The $0.05(Mn(OH)_2)$ @$0.95(Ni_{0.95}Co_{0.05}(OH)_2)$ precursor was mixed with smashed $LiOH · H_2O$ with a molar ratio of Li:Metal = 1.05:1 using a 3D mixer. The mixture was sintered at 480 ℃ for 5 hours followed by 800 ℃ for 16 hours under an oxygen atmosphere. The resultant powder is concentration-gradient $LiNi_{0.9}Co_{0.05}Mn_{0.05}O_2$ (CG-LNCMO) cathode material. For the purpose of comparison, the average concentration $LiNi_{0.9}Co_{0.05}Mn_{0.05}O_2$ (AC-LNCMO) was synthesized with identical procedure with the change in ion solution (1.6 M) containing molar ratio of $NiSO_4·6H_2O$: $CoSO_4·7H_2O$: $MnSO_4·H_2O$ =90：5：5.

2.2. Characterization of physical properties

X-ray diffraction (XRD) analyses were performed using a diffractometer (PANalytical, X’Pert) equipped with a Cu/Ka source. The morphology and atomic concentration of the powders were characterized using a scanning electron microscope (SEM) equipped with an energy dispersive spectroscope (EDS) (S3400N, Hitachi). The overall element content was measured via ICP-OES (Perkin Elmer Optima 2100 DV). The content variation of Mn was determined as follows. A small amount of CG-LNCMO particles and an adequate amount of agate balls were placed in a mill pot that rotated at 100 rpm for 20 minutes through a planetary ball mill (FRITSCH P6, FRITSCH, Germany). The CG-LNCMO particles collided in the pot; the particles broken in half were examined using the SEM. The element content of Mn was analyzed using an EDS from the edge to the center of the rupture surface of the CG-LNCMO particle [32-33].

2.3. Electrochemical measurements

The slurry for the cathode was obtained by mixing the active material, carbon-black (Super P, TIMCAL co.) and KS-4 (TIMCAL co.) at a ratio of 90:2:4 (wt.%) in a 4% polyvinylidene fluoride (PVdF #1300, KUREHA co.)/NMP (MITSUBISHI CHEMICAL co.) solution. The slurry was cast on aluminum foil and dried at 80 ℃ for an hour. The assembly of CR2032-type lithium-ion coin cells using either CG-LNCMO or AC-LNCMO cathode was performed in an argon-filled glovebox (MBRAUNMB 10COMPACT). The electrolyte in the coin cell was 1 M $LiPF_6$ in a 1:1 ethylene carbonate-diethyl carbonate mixed solvent. The initial charge/discharge, high-current discharge, and cycle life tests were performed at room temperature using a battery automation test system (Acu Tech System BAT-750B). The electrochemical impedance spectrometry (EIS) tests were measured using a CHI 614B with an AC frequency within 10^5~10^{-3} Hz with a 5 mV pulse at 4.3 V. In the PITT measurements, I(t) vs. t was measured as a function of potential steps at 30 mV ranging from 3.6 to 4.3 V. Each potential step was applied when the electrode had reached equilibrium, as defined by a residual current of less than 1 μA.

2.4. Thermal evaluation

The cathode samples for the differential scanning calorimetry (DSC) analysis were prepared as follows. Coin cells were initially charged to 4.3 V at a 0.1 C rate and then opened in an argon-filled dry box to remove the charged cathode samples. Approximately 3 mg of the cathode with 3 µL of electrolyte was hermetically sealed in an aluminum pan. DSC scanning was carried out at a scan rate of 5 ºC min^{-1} from 190 ~240 ºC using a Perkin-Elmer DSC7 instrument.

3. RESULTS AND DISCUSSION

3.1 Physical properties

Fig. 1. shows the SEM images of the $Ni_{0.9}Co_{0.05}Mn_{0.05}(OH)_2$ precursor. The spherical secondary particles have diameters of approximately 10~12 μm that form closely packed needle-like primary particles. The spherical shape of the cathode material effectively increases the packing density.

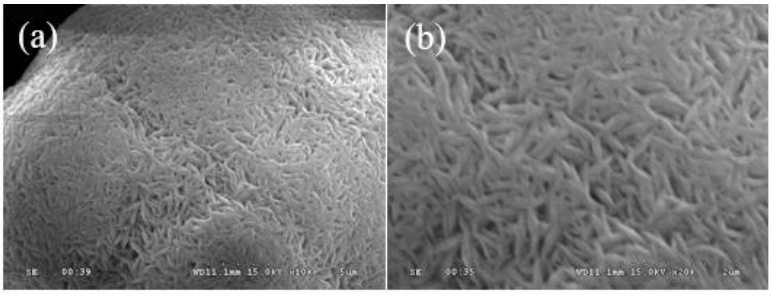

Figure 1. The SEM images of $Ni_{0.9}Co_{0.05}Mn_{0.05}(OH)_2$ at magnitudes of (a)10k and (b)20k

Meanwhile, creating the gradient concentration within a particle during precursor synthesis requires two steps. The first step is to synthesize spherical $Ni_{0.95}Co_{0.05}(OH)_2$ precursor particles through co-precipitation. The SEM images of $Ni_{0.95}Co_{0.05}(OH)_2$ shown in Fig. 2. appear similar to the $Ni_{0.9}Co_{0.05}Mn_{0.05}(OH)_2$ that appears in Fig. 1. The second step is to precipitate $Mn(OH)_2$ on the surface of the suspended $Ni_{0.95}Co_{0.05}(OH)_2$ precursor particles, which results in $0.05(Mn(OH)_2)@0.95(Ni_{0.95}Co_{0.05}(OH)_2)$ particles. As Fig. 3. shows, the secondary particle remains spherical after being coated with $Mn(OH)_2$. However, the needle-like structure is not visible due to the coating of $Mn(OH)_2$.

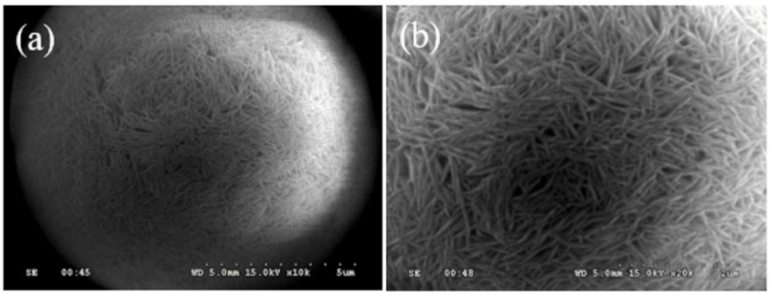

Figure 2. The SEM images of $Ni_{0.9}Co_{0.05}(OH)_2$ at magnitudes of (a) 10k and (b) 20k

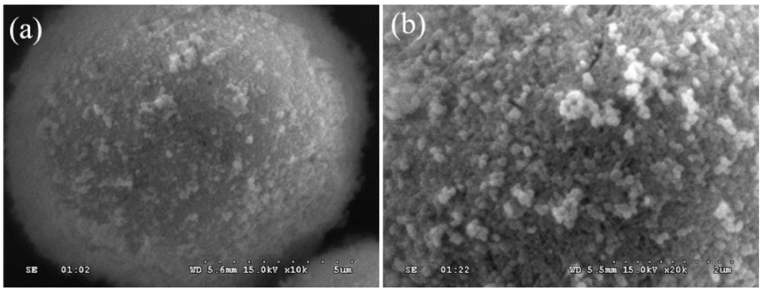

Figure 3. The SEM images of $0.05(Mn(OH)_2)@0.95(Ni_{0.95}Co_{0.05}(OH)_2)$ at magnitudes of (a) 10k and (b) 20k

The as-prepared precursors of $Ni_{0.9}Co_{0.05}Mn_{0.05}(OH)_2$ and $0.05(Mn(OH)_2)@0.95(Ni_{0.95}Co_{0.05}(OH)_2)$ were separately mixed with $LiOH \cdot H_2O$ and sintered using the conditions given above. These two cathode materials are identical in overall chemical composition, but the metal concentrations in particle of both materials are different. The resultant cathode material, $LiNi_{0.9}Co_{0.05}Mn_{0.05}O_2$, has a homogeneous concentration that is denoted as AC-LNCMO. The same chemical composition with a gradient concentration distribution is denoted as CG-LNCMO. Fig. 4. shows the SEM images of these two materials. It is apparent that the needle-like primary structure was transformed to a cubic-like structure after sintered at high temperature. The diameters of the secondary particles remained 10~12 μm.

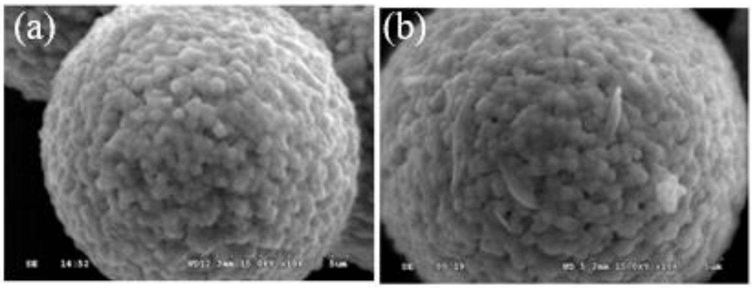

Figure 4. The SEM images of (a) AC-LNCMO and (b) CG-LNCMO

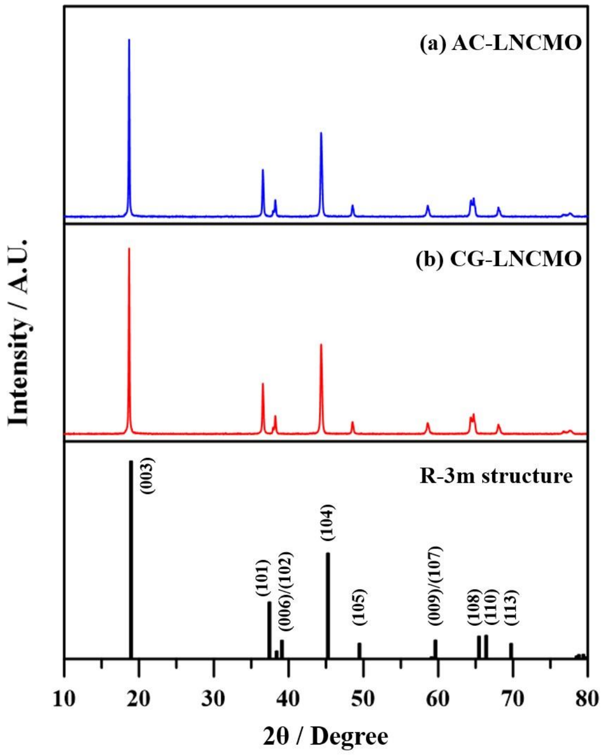

Figure 5. The XRD spectra of AC-LNCMO and CG- LNCMO

Fig. 5. shows the XRD spectra of AC-LNCMO and CG-LNCMO. Referral to the standard spectrum library confirmed that both materials possessed α-$NaFeO_2$ structures and that the space groups were both R-3 m [31,34-35]. According to Bragg's Law and hexagonal crystal structure, lattice constant a (width of lattice) and c (height of lattice) can be calculated. The volume of each lattice can be determined and crystal grain size can be calculated using the Scherer equation. Table 1 summarizes these numbers and shows that a, c, and lattice volume are similar between the two materials. The degree of the cation-mixing of Li^+/Ni^{2+} can be observed by the intensity ratios of (003) and (104) [11,36]. The higher the ratio, the lower the degree of the cation-mixing. The ratio of CG-LNCMO ($I_{003}/I_{104} = 2.06$) is higher than that of AC-LNCMO ($I_{003}/I_{104} = 2.01$). Therefore, CG-LNCMO tends to be more stable during charge/discharge processing.

ICP-OES was used to determine that the overall molar ratio of Ni: Co: Mn in AC-LNCMO was 90.1: 4.8: 5.1. The same ratio determined by EDS was 89.3: 5.7: 5.0. ICP-OES was used to determine that the overall molar ratio of Ni: Co: Mn in CG-LNCMO was 89.2: 4.9: 5.9. The EDS measurement of $0.05(Mn(OH)_2)@0.95(Ni_{0.95}Co_{0.05}(OH)_2)$ precursor showed that the molar ratio of Ni: Co: Mn was 84.5: 2.4: 13.1. The sintered CG-LNCMO showed a Ni: Co: Mn molar ratio of 88.4: 4.1: 7.5. A cross-section EDS experiment was performed to determine the Mn concentration difference between the surface and the core. As shown in Fig. 6., the Mn on the surface gradually diffused into the particle core due to the high temperature and long sintering time, which resulted in a continuous concentration gradient across the particle radius.

Table 1. Lattice parameters of AC-LNCMO and CG-LNCMO

Cathode	Lattice parameter			I_{003}/I_{104}
	a/Å	c/Å	Vol/Å^3	
AC-LNCMO	2.87	14.21	101.54	2.01
CG-LNCMO	2.87	14.24	102.07	2.06

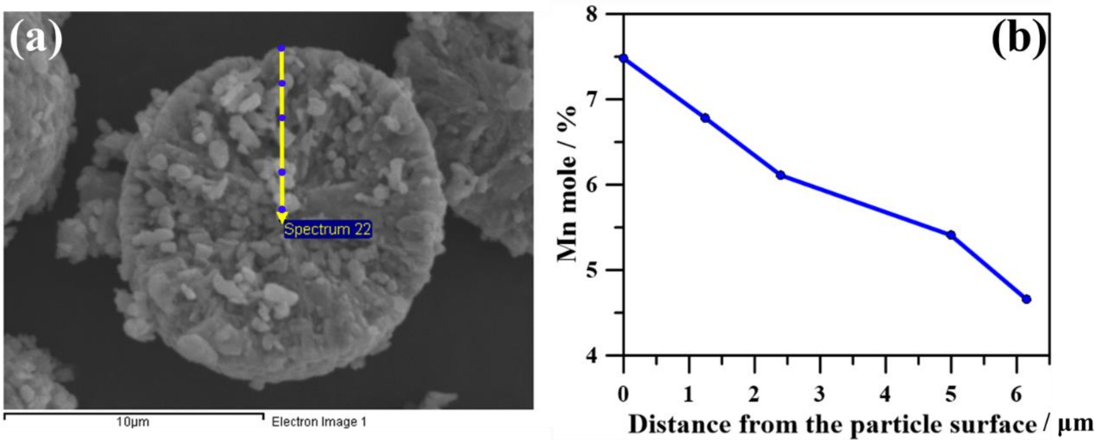

Figure 6. (a)Cross-section SEM image of CG-LNCMO, (b) Mn concentration along the particle radius

3.2 Electrochemical measurements

The different electrochemical behaviors between AC-LNCMO and CG-LNCMO can be seen in the initial charge/discharge curves shown in Fig. 7. The test voltage ranged from 2.8 to 4.3 V. The discharge capacity of AC-LNCMO was 208.93 mAh/g, and the irreversible capacity was 46.81 mAh/g. The discharge capacity of CG-LNCMO was 219.47 mAh/g with an irreversible capacity of 42.30 mAh/g (Table 2.**)**. The higher discharge capacity and smaller irreversible capacity of CG-LNCMO was caused by the high concentration of Mn near the surface and the high concentration of Ni in the inner core [33,37-38]. The strong Mn-O bonds stabilize the surface structure of the material and minimize the reactions between the electrolyte and cathode material. Thus, CG-LNCMO provides better overall electrochemical performance [15,38].

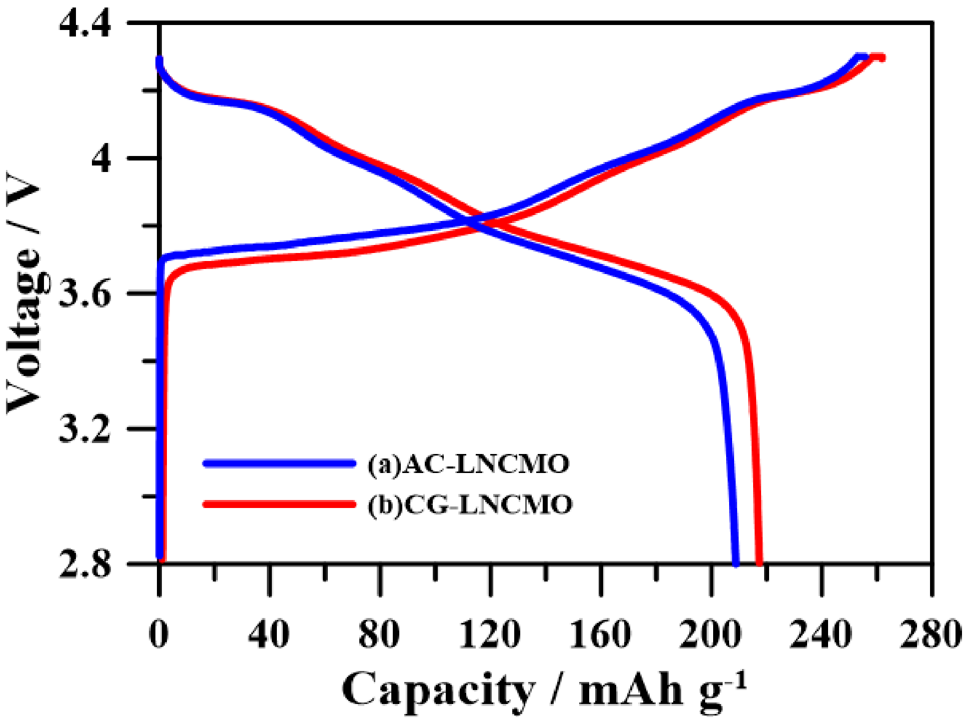

Figure 7. Charge/discharge curves of AC-LNCMO and CG-LNCMO at 0.1 C charge and discharge during the first cycle

Table 2. Comparison of the charge/discharge capacity in the first cycle between AC-LNCMO and CG-LNCMO

	AC-LNCMO	CG-LNCMO
Charge Capacity (mAh/g)	255.74	261.77
Discharge Capacity (mAh/g)	208.93	219.47
Irreversible Capacity (mAh/g)	46.81	42.30

Both materials were charged at a 0.2 C charging rate within a working potential range of 2.8- 4.3 V and then separately discharged at 0.5, 1, 2, 3, 4, and 5 C to test the capacity at different discharge rates. Fig. 8. shows the reduction in capacity as the discharge rate increased. The reduction is caused by the polarization of the electrodes during high-current discharge. Thus, the charge-transfer rate is one of the key factors that dominate the discharge performance of cathode material. The results of discharge at different rates are summarized in Table 3. As the discharge current increased, the discrepancy between AC-LNCMO and CG-LNCMO became more obvious. The high Mn content on the surface of CG-LNCMO can inhibit the cation-mixing of Li^+/Ni^{2+} [9], which stabilizes the surface structure, and lowers the charge-transfer resistance (R_{ct}). Therefore, GC-LNCMO showed superior discharge performance over AC-LNCMO when tested under higher current densities.

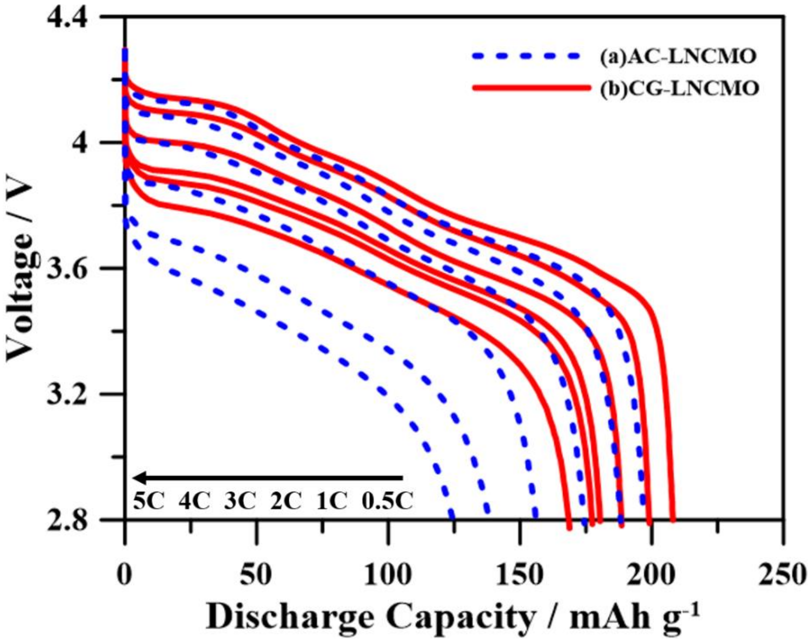

Figure 8. Discharge curves for AC-LNCMO and CG-LNCMO under different current densities

Table 3. Comparison of the discharge capacity between AC-LNCMO and CG-LNCMO under high current discharge

	AC-LNCMO		CG-LNCMO	
	Discharge Capacity (mAh/g)	Capacity Retention (%)	Discharge Capacity (mAh/g)	Capacity Retention (%)
0.5C	197.07	100	208.04	100
1C	188.25	95.52	199.06	95.67
2C	174.42	88.51	188.55	90.63
3C	156.17	79.40	180.60	86.81
4C	138.38	70.22	177.46	85.30
5C	124.74	63.30	168.77	81.12

Fig. 9. shows the decay in capacity for both materials after 40 cycles of charge/discharge. The capacity of AC-LNCMO appears to decay significantly more than that of CG-LNCMO. As Table 4 shows, AC-LNCMO retained an 81.36% capacity after 40 cycles while CG-LNCMO retained a 95.61%

capacity. It is obvious that improving the stability in the surface structure of concentration-gradient material mitigates the erosion by electrolytes and improves cycle life [23,39].

For Ni-rich cathode material (Ni≧0.9) with a concentration-gradient structure, Sun et al. [40,41] have proposed the core-shell gradient (CSG) cathode materials (CSG-$LiNi_{0.9}Co_{0.05}Mn_{0.05}O_2$ and CSG-$LiNi_{0.95}Co_{0.25}Mn_{0.25}O_2$), and those were synthesized using the core-shell $Ni_{0.8}Co_{0.1}Mn_{0.1}(OH)_2/Ni(OH)_2$ precursors. A core-shell gradient cathode significantly enhances cycling stability due to protection by the micron-sized shell when compared with the core component. In this work, a Ni-rich cathode material with a continuous concentration-gradient structure of $LiNi_{0.9}Co_{0.05}Mn_{0.05}O_2$ was successfully synthesized using a $Mn(OH)_2$-coated $Ni_{0.95}Co_{0.05}(OH)_2$ precursor. The continuous concentration-gradient cathode material also has structural stability, high capacity, and good cycle-life. These improved results are similar to those found by Sun et al. [40,41].

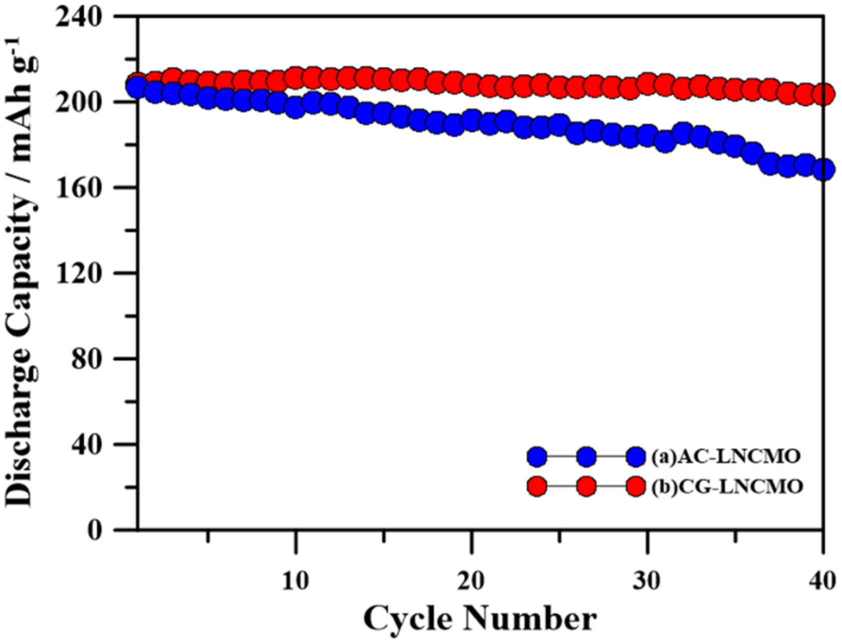

Figure 9. Cycling performances of the AC-LNCMO and CG-LNCMO at 0.2 C charge and 0.5 C discharge

Table 4. Comparing the capacities of AC-LNCMO and CG-LNCMO after the 1st, 10th, 20th, 30th, and 40th cycles

	AC-LNCMO		CG-LNCMO	
	Discharge Capacity (mAh/g)	Capacity Retention (%)	Discharge Capacity (mAh/g)	Capacity Retention (%)
1st	207.17	100.0	211.18	100.0
10th	197.66	95.41	208.42	98.69
20th	191.45	92.41	208.02	98.50
30th	184.07	88.85	203.42	96.33
40th	168.55	81.36	201.91	95.61

3.3 EIS analysis

We used a two-electrode method for EIS analysis. The lithium metal served as both the anode and the reference electrode. The electrodes were coated with either AC-LNCMO or CG-LNCMO and used as cathodes. The scanning frequency, pulse, and potential are mentioned in the experimental section.

Fig. 10. is the simulated equivalent circuit for AC-LNCMO and CG-LNCMO battery impedance analysis. Where R_s is the resistance of the electrolyte solution between electrodes. R_f is the resistance of the surface layer. R_{ct} is the charge-transfer resistance while Li-ion enters the electrode material. CPE1 and CPE2 are simulated capacity elements. W is the diffusive impedance of Li-ion [42].

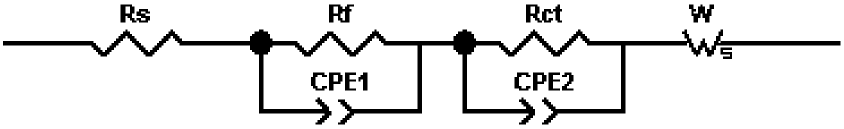

Figure 10. The equivalent circuit of a cathode electrode

Fig. 11. shows the Nyquist plot of impedance analysis for Li-ion batteries using two different cathode materials. In this figure both materials show two semicircles. The resistance values were calculated using equivalent circuitry simulation, as listed in Table 5.

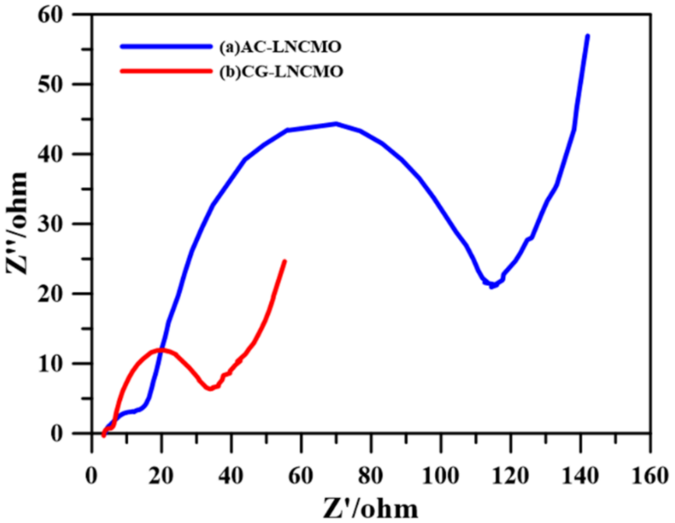

Figure 11. Nyquist plot of the Li/AC-LNCMO cell and Li/CG-LNCMO cell after a first charge

Both AC-LNCMO and CG-LNCMO react with electrolytes and form a passivation layer after the first charge/discharge cycle. CG-LNCMO contains a higher number of Mn on the particle surface. The strong Mn-O bonding helps stabilize the surface structure [43] and mitigates the formation of the passivation layer, which means the side reaction between the electrolyte and material surface was suppressed. The thinner passivation layer also improves the charge-transfer efficiency, which results in lower values for R_f and R_{ct}.

Table 5. Impedance analysis of AC-LNCMO and CG-LNCMO

	AC-LNCMO	CG-LNCMO
R_f (Ω)	14.2	2.8
R_{ct} (Ω)	100.8	27.9

3.4. Determination of the lithium-ion diffusion coefficient

The migration of Li-ions in the cathode electrode is affected mainly by the rate of Li-ions intercalated into the lattice of metal oxide. In order to calculate the apparent chemical diffusion coefficient (D_{app}) of Li-ions from PITT, the thickness of the electrode (l) was used as the characteristic diffusion length.

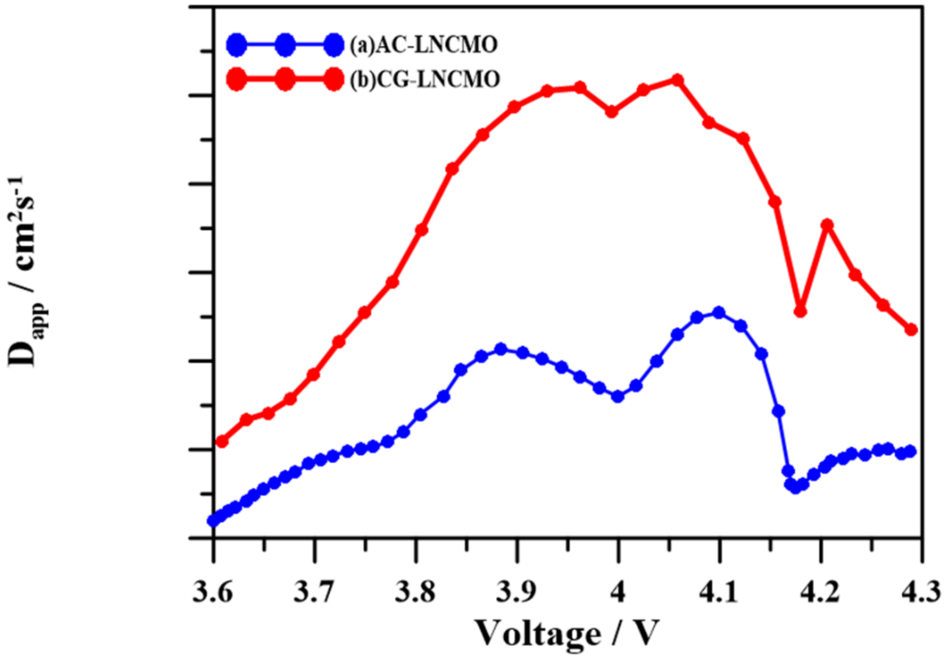

Figure 12. Apparent chemical diffusion coefficient (D_{app}) calculated from PITT measurement in Li/AC-LNCMO and Li/CG-LNCMO cells.

The apparent chemical diffusion coefficient (D_{app}) was estimated from the slope of ln $I(t)$ vs. t plot and can be expressed by the following finite-diffusion equation with a long-time definition: $t \gg l^2/D_{app}$ [44].

$$I(t) = \frac{2nFAD_{app}C^*}{l}\exp\left(\frac{-\pi^2 D_{app}}{4l^2}t\right)\ t >> \frac{l^2}{D_{app}}$$

Fig. 12. shows the variations in the apparent chemical diffusion coefficients (D_{app}) of Li-ions moving out of the LNCMO with the applied potentials during the de-intercalation process. The D_{app} of CG-LNCMO was higher than that of AC-LNCMO. The higher mass-transfer rate of CG-LNCMO also accounts for its better rate capability, according to the higher concentration of Mn on the surface that effectively suppressed the side reactions with the electrolyte and enhanced the diffusion of Li-ions.

3.5. Thermal stability measurements

Fig. 13. shows the DSC data of the AC-LNCMO and CG-LNCMO cells charged to 4.3V. The exothermic heat was due to the reaction of oxygen from the decomposed cathode oxide with the electrolyte.

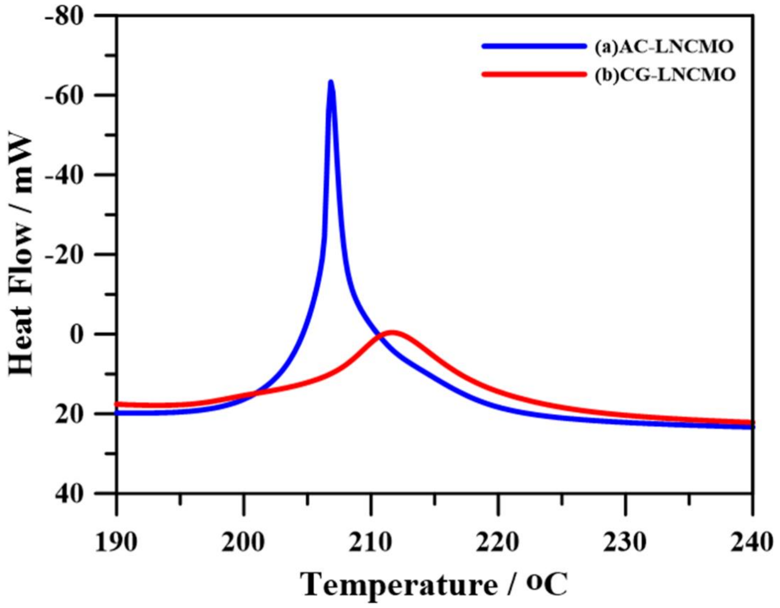

Figure 13. DSC profiles of AC-LNCMO and CG-LNCMO cells charged at 4.3 V.

Table 6. DSC analysis of AC-LNCMO and CG-LNCMO

	AC-LNCMO	**CG-LNCMO**
DSC Peak (℃)	206.83	211.67
Exothermic heat(J/g)	804.54	590.42

Table 12. shows that the exothermic peak of the AC-LNCMO electrode occurred at about 206.83 ℃, and the reaction heat was 804.54 J g^{-1}, compared with 211.67 ℃ and 590.42 J g^{-1} for the CG-

LNCMO. This result shows that the CG-LNCMO has better thermal stability than the AC-LNCMO [45-48]. This was attributed to the stable manganese oxide that further improved the thermal stability of the gradient cathode material [49,50].

4. CONCLUSIONS

In this work we produced a continuous concentration gradient structure to improve the stability of $LiNi_{0.9}Co_{0.05}Mn_{0.05}O_2$ nickel-rich cathode material. CG-LNCMO was successfully synthesized via co-precipitation and sinter processes, which resulted in a sufficiently high concentration of Mn on the particle surface. By comparison with homogeneous AC-LNCMO, X-ray diffraction confirmed that both materials belong to the same lattice. The results of ICP-OES and cross-section EDS showed that CG-LNCMO possesses a higher Mn content on its surface, which reduces reactions with electrolytes and results in better stability for the surface structure. The electrochemical performances of Li-ion coin cells using CG-LNCMO and AC-LNCMO were investigated. The CG-LNCMO has a higher reversible capacity and a smaller irreversible capacity in the first cycle. In the test of high-current discharge, the stability of the CG-LNCMO surface reduces the material impedance and the potential drop. Therefore, CG-LNCMO shows a better discharge capacity under high-current operation. In addition, the concentration gradient of Mn also reduces the side reactions between electrode material and electrolytes, which significantly prolongs the cycle life of cathode material. The EIS and PITT analyses demonstrated that the resistance of CG-LNCMO is much lower than that of AC-LNCMO and a higher mass-transfer rate can be achieved.

ACKNOWLEDGEMENTS
The authors would like to thank the Industrial Technology Research Institute of Taiwan for financial support of this work.

References

1. R. Reinhardt, B. Amante García, L. Canals Casals and S. Gassó Domingo, *Proj. Manag. and Engineering Research,* (2018) 99.
2. M. N. Obrovac, O. Mao, and J. R. Dahn, *Solid State Ionics,* 112 (1998) 9.
3. H. W. Yan, X. J. Huang, Z. H. Lu, H. Huang, R. J. Xue, and L. Q. Chen, *J. Power Sources,* 68 (1997) 530.
4. Z. S. Peng, C.R. Wan, and C.Y. Jiang, *J. Power Sources,* 72 (1998) 215.
5. H. J. Arai, S. G. Okada, Y. J. Sakurai, and J. I. Yamaki, *Solid State Ionics,* 95 (1997) 275.
6. E. S. Cho, S. W. Seo, and K. M. Min, *ACS Appl. Mater. Interfaces,* 9 (2017) 33257.
7. K. Dokko, S. Horikoshi, T. Itoh, M. Nishizawa, M. Mohamedi, and I. Uchida, *J. Power Sources,* 90 (2000) 109.
8. S. M. Bak, E. Hu, Y. Zhou, X. Yu, D. S. Sanjaya, S. J. Cho, K. B. Kim, K. Y. Chung, X. Q. Yang, and K. W. Nam, *ACS Appl. Mater. Interfaces,* 6 (2014) 22594.
9. C. Liang, F. Kong, R. C. Longo, S. Kc, J. S. Kim, S. Jeon, S. A. Choi, and K. Cho, *J. Phys. Chem. C,* 120 (2016) 6383.
10. J. Zheng, W. H. Kan, and A. Manthiram, *ACS Appl. Mater. Interfaces,* 7 (2015) 6926.

11. H. J. Noh, S. Youn, C. S. Yoon, and Y. K. Sun, *J. Power Sources,* 233 (2013) 121.
12. S. H. Lee, S. Lee, B. S. Jin, and H. S. Kim, *Int. J. Hydrog. Energy,* 44 (2019) 13684.
13. Y. Liu, W. Yao, C. Lei, Q. Zhang, S. W. Zhong, and Z. Yan, *J. Electrochem. Soc.,* 166 (2019) A1300.
14. K. K. Cheralathan, N. Y. Kang, H. S. Park, Y. J. Lee, W. C. Choi, Y. S. Ko, and Y. K. Park, *J. Power Sources,* 195 (2010) 1486.
15. C. S. Yoon, H. H. Ryu, G. T. Park, J. H. Kim, K. H. Kim, and Y. K. Sun, *J. Mater. Chem. A,* 6 (2018) 4126.
16. D. Sivlin, and O. Keles, *TMS Annual Meeting & Exhibition,* (2018) 515.
17. S. J. Sim, S. H. Lee, B. S. Jin, and H. S. Kim, *Sci. Rep.,* 9 (2019) 8952.
18. Y. Lv, X. Cheng, W. Qiang, and B. Huang, *J. Power Sources,* 450 (2020) 227718.
19. G. Shang, Y. Tang, Y. Lai, J. Wu, X. Yang, H. Li, C. Peng, J. Zheng, and Z. Zhang, *J. Power Sources,* 423 (2019) 246.
20. A. Chakraborty, S. Kunnikuruvan, M. Dixit, and D. T. Major, *Isr. J. Chem.,* 60 (2020) 850.
21. H. Yang, H. H. Wu, M. Ge, L. Li, Y. Yuan, Q. Yao, J. Chen, L. Xia, J. Zheng, Z. Chen, J. Duan, K. Kim, X. C. Zeng, W. K. Lee, Q. Zhang, and J. Lu, *Adv. Funct. Mater,* 29 (2019) 1808825.
22. H. Kim, S. B. Kim, D. H. Park, and K. W. Park, *Energies,*13 (2020) 4808.
23. B. B. Lim, S. J. Yoon, K. J. Park, C. S. Yoon, S. J. Kim, J. J. Lee, and Y. K. Sun, *Adv. Funct. Mater.,* 25 (2015) 4673.
24. K. J. Park, B. B. Lim, M. H. Choi, H. G. Jung, Y. K. Sun, M. Haro, N. Vicente, J. Bisquert, and G. Garcia-Belmonte, *J. Mater. Chem. A,* 3 (2015) 22183.
25. Y. K. Sun, B. R. Lee, H. J. Noh, H. Wu, S. T. Myung, and K. Amine, *J. Mater. Chem.,* 21 (2011) 10108.
26. Y. K. Sun, D. H. Kim, C. S. Yoon, S. T. Myung, J. Prakash, and K. Amine, *Adv. Funct. Mater,* 20 (2010) 485.
27. P. Hou, H. Zhang, Z. Zi, L. Zhang, and X. Xu, *J. Mater. Chem. A,* 5 (2017) 4254.
28. J. Y. Liao, and A. Manthiram, *J. Power Sources,* 282 (2015) 429.
29. L. W. Liang, K. Du, Z. D. Peng, Y. B. Cao, and G. R. Hu, *Chin. Chem. Lett.,* 25 (2014) 883.
30. M. H. Lee, Y. J. Kang, S. T. Myung, and Y. K. Sun, *Electrochim. Acta,* 50 (2004) 939.
31. D. L. Vu, and J. W. Lee, *Korean J. Chem. Eng.,* 33 (2016) 514.
32. M. H. Liu, H. T. Huang, C. M. Lin, J. M. Chen, and S. C. Liao, *Electrochim. Acta*, 120 (2014) 133.
33. M. H. Liu, C. W. Jen, J. M. Chen, and S. C. Liao, *Int. J. Electrochem. Sci.*, 13 (2018) 4350.
34. J. Zheng, W. Zhou, Y. Ma, H. Jin, and L. Guo, *J. Alloys Compd.*, 635 (2015) 207.
35. Y. K. Sun, S. T. Myung, M. H. Kim, J. Prakash, and K. Amine, *J. Am. Chem. Soc.,* 127 (2005) 13411.
36. F. Schipper, E. M. Erickson, C. Erk, J. Y. Shin, F. F. Chesneau, and D. Aurbacha, *J. Electrochem. Soc.,* 164 (2017) A6220.
37. J. L. Shi, R. Qi, X. D. Zhang, P. F. Wang, W. G. Fu, Y. X. Yin, J. Xu, L. J. Wan, and Y. G. Guo, *ACS Appl. Mater. Interfaces*, 9 (2017) 42829–42835.
38. K. Min, C. Jung, D. S. Ko, K. Kim, J. Jang, K. Park, and E. Cho, *ACS Appl. Mater. Interfaces,* 10 (2018) 20599.
39. G. W. Yoo, B. C. Jang, and J. T. Son, *Ceram. Int.,* 41 (2015) 1913.
40. U. H. Kim, H. H. Ryu, J. H. Kim, R. Mücke, P. Kaghazchi, C. S. Yoon and Y. K. Sun, *Adv. Energy Mater.,* 9 (2019) 1803902.
41. D. W. Jun, C. S. Yoon, U. H. Kim and Y. K. Sun, *Chem. Mater.,* 29 (2017) 5048.
42. Q. Zhang, Y. Su, L. Chen, Y. Lu, L. Bao, T. He, J. Wang, R. Chen, J. Tan, and F. Wu, *J. Power Sources,* 396 (2018) 734.
43. L. Li, Q. Yao, H. Zhu, Z. Chen, L. Song, and J. Duan, *J. Alloys and Compd.*, 686 (2016) 30.
44. J. J. Zhang, P. He, and Y. Y. Xia, *J. Electroanal. Chem.,* 624 (2008) 161.
45. Z. D. Huang, K. Zhang, T. T. Zhang, R. Q. Liu, X. J. Lin, Y. Li, T. Masese, X. Liu, X. M. Feng, and Y. W. Ma, *Energy Stor. Mater.,* 5 (2016) 205.
46. K. W. Nam, S. M. Bak, E. Hu, X. Yu, Y. Zhou, X. Wang, L. Wu, Y. Zhu, K. Y. Chung, and X. Q.

Yang, *Adv. Funct. Mater.,* 23 (2013) 1047.
47. P. Hou, F. Li, Y. Sun, H. Li, X. Xu, and T. Zhai, *ACS Appl. Mater. Interfaces,* 10 (2018) 24508.
48. K. J. Park, M. J. Choi, F. Maglia, S. J. Kim, K. H. Kim, C. S. Yoon, and Y. K. Sun, *Adv. Energy Mater.,* 8 (2018) 1703612.
49. J. Xiao, N. A. Chernova, and M. S. Whittingham, *Chem. Mater.,* 22 (2010) 1180.
50. H. Shi, X. Wang, P. Hou, E. Zhou, J. Guo, J. Zhang, D. Wang, F. Guo, D. Song, X. Shi, and L. Zhang, *J. Alloys Compd.,* 587 (2014) 710.